

AN ICE GIANT EXOPLANET INTERPRETATION OF THE ANOMALY
IN MICROLENSING EVENT OGLE-2011-BLG-0173

RADOSŁAW POLESKI,^{1,2} B. S. GAUDI,¹ A. UDALSKI,² M. K. SZYMAŃSKI,² I. SOSZYŃSKI,²
P. PIETRUKOWICZ,² S. KOZŁOWSKI,² J. SKOWRON,² Ł. WYRZYKOWSKI,² AND K. ULACZYK^{2,3}

¹*Department of Astronomy, Ohio State University, 140 W. 18th Ave., Columbus, OH 43210, USA*

²*Warsaw University Observatory, Al. Ujazdowskie 4, 00-478 Warszawa, Poland*

³*Department of Physics, University of Warwick, Coventry CV4 7AL, UK*

(Received XXX; Revised XXX; Accepted XXX)

Submitted to ApJ

ABSTRACT

We analyze the microlensing event OGLE-2011-BLG-0173, which shows a small perturbation at the end of the microlensing event caused by the primary lens. We consider both binary lens and binary source models and we explore their degeneracies, some of which have not previously been recognized. There are two families of binary lens solutions, one with a mass ratio $q \approx 4 \times 10^{-4}$ and a separation $s \approx 4.6$ and the other with $q \approx 0.015$ and $s \approx 0.22$, i.e, both have companions in the planetary regime. We search for solutions by using Bayesian analysis that includes planet frequency as a prior and find that the $s \approx 4.6$ family is the preferred one with $\approx 4 M_{\text{Uranus}}$ mass planet on an orbit of ≈ 10 AU. The degeneracies arise from a paucity of information on the anomaly, demonstrating that high-cadence observations are essential for characterizing wide-orbit microlensing planets. Hence, we predict that the planned WFIRST microlensing survey will be less prone to these degeneracies than the ongoing ground-based surveys. We discuss the known low-mass, wide-orbit companions

Corresponding author: Radosław Poleski

poleski.1@osu.edu

and we notice that for the largest projected separations the mass ratios are either high (consistent with brown dwarf companions) or low (consistent with Uranus analogs), but intermediate mass ratios (Jupiter analogs on wide orbits) have not been detected to date, despite the fact that the sensitivity to such planets should be higher than that of Uranus analogs. This is therefore tentative evidence of the existence of a massive ice giant desert at wide separations. On the other hand, given their low intrinsic detection sensitivity, Uranus analogs may be ubiquitous.

Keywords: gravitational lensing: micro — planets and satellites: detection — brown dwarfs

1. INTRODUCTION

Our knowledge of the formation of the outer members of planetary systems is very limited. Even in the case of our own solar system, we lack a full understanding of how and when Uranus and Neptune formed and migrated to their current orbits (e.g., [Pollack et al. 1996](#); [Thommes et al. 1999](#); [Goldreich et al. 2004](#); [Tsiganis et al. 2005](#)). Among analogs to the known planets in our solar system, ice giant planets are particularly hard to detect using conventional techniques (e.g. [Kane 2011](#)), due to their faintness in reflected light or thermal emission, their relatively low mass, and, most importantly, their large semi-major axes and longer periods. There are two planet detection techniques that in principle allow one to detect planets on wide orbits: direct imaging and gravitational microlensing. Directly detecting ice giant analogs in mature systems in reflected light is exceptionally challenging because of their low planet-to-star flux ratios. For example, the planet-to-star flux ratio is $\sim \text{few} \times 10^{-11}$ in reflected light for a Uranus/Sun analog.

The gravitational microlensing technique is sensitive to the mass of the light-bending body, thus providing means for finding planets on very wide orbits even if their luminosities are low. The upcoming Wide-Field Infrared Survey Telescope (WFIRST) mission ([Spergel et al. 2015](#); [Penny et al. 2018](#)) will give us unprecedented opportunity to study the ice giant planets. The major disadvantage of the microlensing - its unpredictability and non-repetitiveness - will be overcome by WFIRST by collecting high-cadence (15 min.) continuous observations over relatively long periods of time (6 seasons of 72 days each). In some cases, WFIRST will observe the planetary anomaly but will not observe the peak of the host subevent owing to the long time separation of the two peaks. Nevertheless, in most cases the basic planetary parameters should be constrained thanks to the large number of WFIRST epochs or the ground-based observations of the host subevent peak.

While the WFIRST survey will definitely change our understanding of outer planets in planetary systems, we can and should use existing facilities to study the ice giant planets to the extent possible. The studies that are possible with existing facilities can give us first estimates of the ice giant planet occurrence rates and can help in developing the WFIRST program by: 1) identifying optimal survey strategies, as well as precursor and concurrent observations, and 2) identifying and solving difficulties

and degeneracies in detecting and characterizing planets via microlensing for such systems. Among existing facilities, the Korean Microlensing Telescope Network (KMTNet; Kim et al. 2016, 2018b) is suited best because of the 24-hour coverage allowed by the three identical telescopes at different longitudes.

Here we present an analysis of the anomalous microlensing event OGLE-2011-BLG-0173. Several degenerate models are found, and our analysis indicates that the preferred explanation of the anomaly is a model with a single source and a lens system being a star with a planet on an extremely wide orbit. The planet-to-host mass ratio is a few times 10^{-4} and the on-sky-projected separation is almost five times larger than the angular Einstein ring radius, which is the typical angular distance at which planetary perturbations are found. These properties are similar to OGLE-2008-BLG-092LAb (Poleski et al. 2014) and make these two planets unique approximate analogs of solar system ice giants. We analyze the existing data for OGLE-2011-BLG-0173 in detail and uncover a number of degeneracies, implying that high-cadence, long-term photometric monitoring is crucial to precisely model events due to ice giant analogs.

In the next Section, we present available observations of OGLE-2011-BLG-0173. Section 3 presents the microlensing model fitting. In Section 4, we estimate the posterior physical properties and compare degenerate models. We discuss occurrence rates of microlensing ice giant exoplanets in Section 5. A summary of our results is presented in Section 6.

2. OBSERVATIONS

The microlensing event OGLE-2011-BLG-0173 occurred at the equatorial coordinates R.A. = $17^{\text{h}}57^{\text{m}}15^{\text{s}}.78$, Dec. = $-28^{\circ}14'01''.9$ and was identified by the Optical Gravitational Lensing Experiment (OGLE) Early Warning System (Udalski 2003). The observations were collected by the 1.3-m Warsaw Telescope situated at Las Campanas Observatory, Chile. The telescope is equipped with a mosaic CCD camera with a field of view of 1.4 deg^2 (Udalski et al. 2015a). The pixel scale is $0''.26$ and typical seeing is $1''.1$. The majority of the OGLE images are collected in the I band and here we use only these data to fit the microlensing model. The additional V -band data do not cover the anomaly part of the light curve. During the 2011 bulge season, OGLE observed the OGLE-2011-BLG-0173

field with a cadence of 20 min, and 2022 *I*-band epochs were collected that year. There were 14 and 12 data points collected during the first and second night of the anomaly, respectively. We also analyzed 909 epochs from the second half of the 2010 bulge season to determine a reliable baseline brightness. There were 27 *V*-band epochs in 2011, which we supplemented with 35 epochs from 2010 and 2012. The photometry of the OGLE images was performed using the difference image analysis technique (Alard 2000; Woźniak 2000). The raw uncertainties in difference image photometry are often underestimated, and thus we corrected them following Skowron et al. (2016).

The baseline brightness in the standard photometric system is $I = 15.968$ mag and $(V - I) = 2.147$ mag. There is an additional star only $0''.55$ away that is fainter by $\Delta I = 1.1$ mag.

The event OGLE-2011-BLG-0173 was also independently discovered by the Microlensing Observations in Astrophysics (MOA) survey (Bond et al. 2001) as MOA-2011-BLG-133. MOA did not collect any useful data during the anomaly due to bad weather (Suzuki et al. 2016) and hence, we do not analyze MOA data. We searched for other time-series photometry for this event that was taken during the anomaly, but none was found.

3. LIGHT-CURVE ANALYSIS

The majority of the event light curve appears to be a standard point-source/point-lens (PSPL) microlensing light curve (Paczynski 1986) with a peak at $\text{HJD}' \equiv \text{HJD} - 2450000 = 5689$, a timescale of 30 days, with the exception of a few-day-long anomaly centered at $\text{HJD}' = 5816$ (see Figure 1). The PSPL model gives a fit worse by $\Delta\chi^2 \approx 340$ compared to the more advanced models presented below, and 50 consecutive points taken over four nights are brighter than the PSPL model. Hence, the anomaly detection is secure. The observed amplitude of the anomaly in the OGLE data is small (≈ 0.03 mag), however, the peak amplitude is not known because it clearly happened when the bulge was not observable from Chile.

The anomalous nature of the event was not recognized while the event was ongoing. This is because the anomaly was brief and did not occur when the source was significantly magnified by the primary lens, and thus the event was close to its baseline brightness and not noticeably magnified outside of the two nights when the anomaly occurred. Such short-timescale anomalies that occur when the

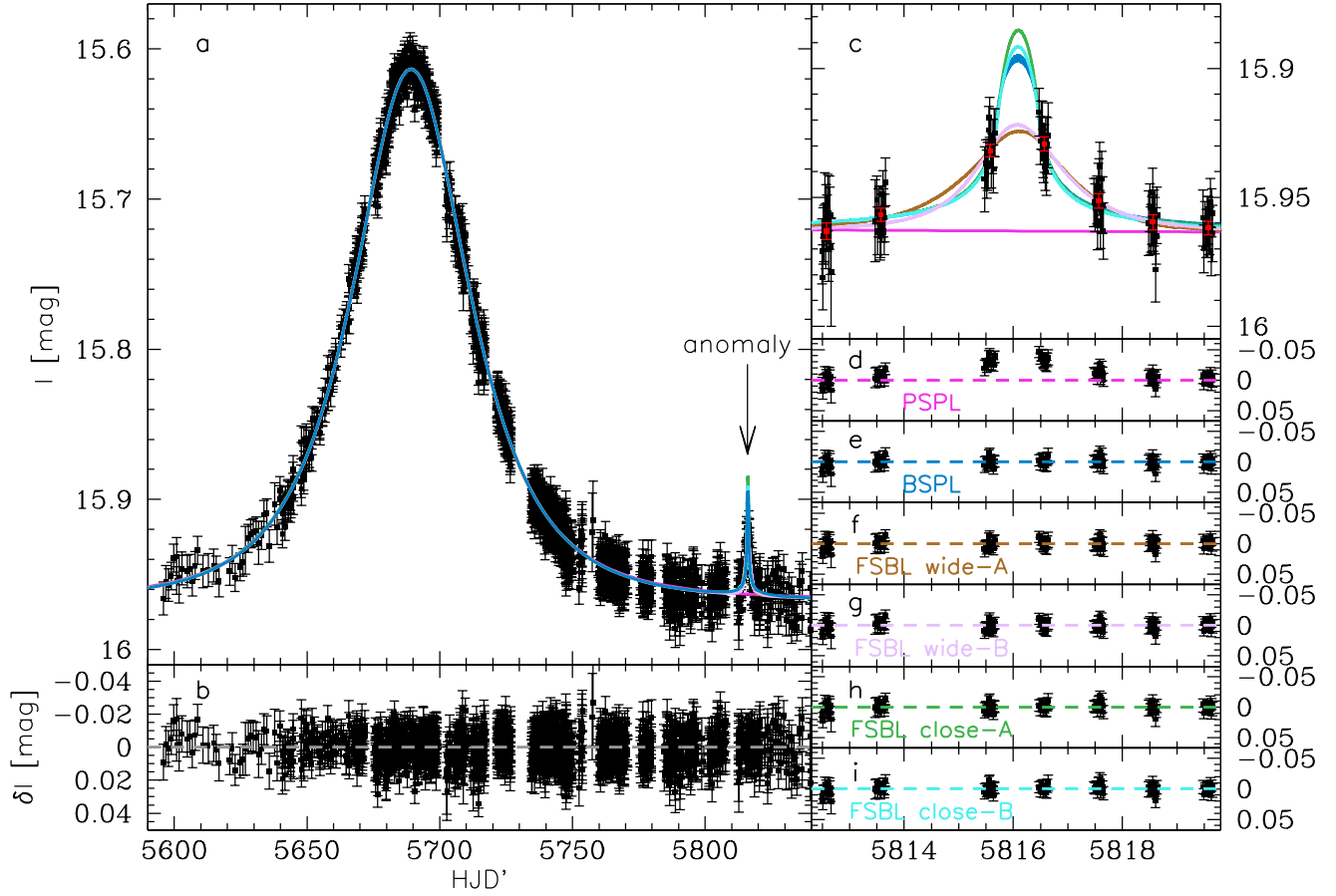


Figure 1. Light curve of microlensing event OGLE-2011-BLG-0173. Panel *a* shows the majority of the primary event along with the anomaly. Black points show the I -band magnitude as a function of $\text{HJD}' = \text{HJD} - 2450000$ in the native cadence of ~ 20 minutes. The solid lines are the various model fits to the data, described below. Panel *c* shows a zoom-in on the anomaly, where the black points are the native sampling and the red points are nightly averages of roughly a dozen individual points. The colored solid lines indicate the models fit to the anomaly: PSPL – magenta, binary source – blue, binary lens wide-A – brown, binary lens wide-B – lavender, binary lens close-A – green, and binary lens close-B – cyan. The residuals from these models are plotted in panels *d-i*, respectively. Residuals shown in panel *b* are for the binary lens close model, but different models do not differ except for the anomaly. The data used to create this figure are available.

source is not significantly magnified are often missed in real time because of a focus on the anomalies close to the time when events peak.

The shape of the anomaly appears to be similar to a second point-lens event with a shorter timescale, either with a point source (PSPL) or a finite source (FSPL). There are two physical situations that can create a microlensing event such as OGLE-2011-BLG-0173, which can essentially be described by two well-separated brightenings, both of which are consistent with being caused by an isolated lens. The first case is if a double source is magnified by a single lens (Griest & Hu 1992; Gaudi 1998). The second case is if a single source is magnified by a lens system composed of two bodies. The possible degeneracy of these two scenarios, particularly those for which the two brightenings had very different timescales, was recognized and analyzed by Gaudi (1998). However, for OGLE-2011-BLG-0173, each scenario also shows additional degeneracies that have not been identified before. We discuss the fits to the binary source and binary lens models below. In both cases we tried to fit models that included the microlensing parallax effect, but due to a large impact parameter (u_0) and relatively short Einstein timescale (t_E), no meaningful constraints on microlensing parallax were found. Hence, in this case, the microlensing model alone does not lead to a direct measurement of the lens mass (Gould 2000).

3.1. Binary source model

The Einstein timescale of the event depends on the lens mass, distances to the lens and the source, and the relative lens—source proper motion. For a binary source event, all these quantities are the same for both stars, hence, the Einstein timescale must be the same for each subevent (though see Han et al. 2017a). The apparent duration of the second subevent in OGLE-2011-BLG-0173 of ≈ 2 days is much shorter than the duration of the first subevent. The subevent duration comparison leads to the conclusion that for a double-source model the second source must be both significantly more blended¹ and fainter than the first source (Gaudi & Gould 1997). High blending requires a very close approach of the lens to the second source (i.e., $u_{0,2} \ll 1$). The very close approach requires including the finite-source effect in the calculations, even though the data do not cover the time of minimum separation. We evaluated the finite-source magnification based on Gould (1994) and Yoo

¹ For binary source models, each source is blended by the blending flux and the other source flux.

et al. (2004) prescriptions. First, we fitted the model without accounting for the limb darkening. The double-source model is characterized by: four parameters characterizing the minimum approach to both sources (epochs – $t_{0,1}$ and $t_{0,2}$; separations – $u_{0,1}$ and $u_{0,2}$) as well as t_E , and ρ_2 (the radius of the second source relative to the characteristic scale of the microlensing event θ_E). Additionally, two source fluxes and a blending flux are found for each model via linear regression. To fit the data, we used the Multimodal Ellipsoidal Nested Sampling algorithm, or MULTINEST (Feroz & Hobson 2008; Feroz et al. 2009).

The first fits that included the finite-source effect and did not include limb darkening revealed two degenerate binary source models. The first model has ρ_2 close to zero, and the second one has $\rho_2 \approx 0.019$ (see Figure 2). The χ^2 for both models is similar, but between the two ρ modes the χ^2 values are larger by up to 3.1 and the highest values are found at $\rho_{2,\text{lim}} = 0.0174$. The magnification of the second source rises and falls more steeply for models without limb darkening than for models with limb darkening. However, on neither of the two anomaly nights does the light curve show a significant slope. The source diameter crossing time is $2\rho_2 t_E = 1.0$ day for $\rho_{2,\text{lim}}$. Hence, the models with $\rho_2 \approx \rho_{2,\text{lim}}$ show slightly higher χ^2 and produce discreet degeneracy. Models with $\rho_2 > \rho_{2,\text{lim}}$ predict an unreasonably small mean value and range of the lens—source relative proper motion: $\mu = \theta_{*,2}/(\rho_2 t_E) = 0.108 \pm 0.016$ mas yr⁻¹ (for determination of angular source radius $\theta_{*,2}$ see below). The two models effectively merge into a single model after the limb-darkening effect is included because the rising and falling wings of the anomaly are less steep for $\rho_2 > 0$ when finite-source effects are included. We assumed a linear limb-darkening coefficient of $u = 0.33$. To find this value, we used Claret & Bloemen (2011) tables and assumed I -band absolute brightness of $M_{I,2} = 8.3$ mag, which results from the preliminary fitted model and analysis of the color-magnitude diagram (CMD; see details below). Table 1 gives results of the binary source fitting. We separately fitted the model with $\rho_2 = 0$ and found that it is worse by $\Delta\chi^2 = 0.31$ compared to the model presented in Table 1.

The amount of blending light we observe, corresponding to $I = 17.839$ mag, is too large to be fully produced by the lens. The blending light could be attributed to a wide-orbit companion to the

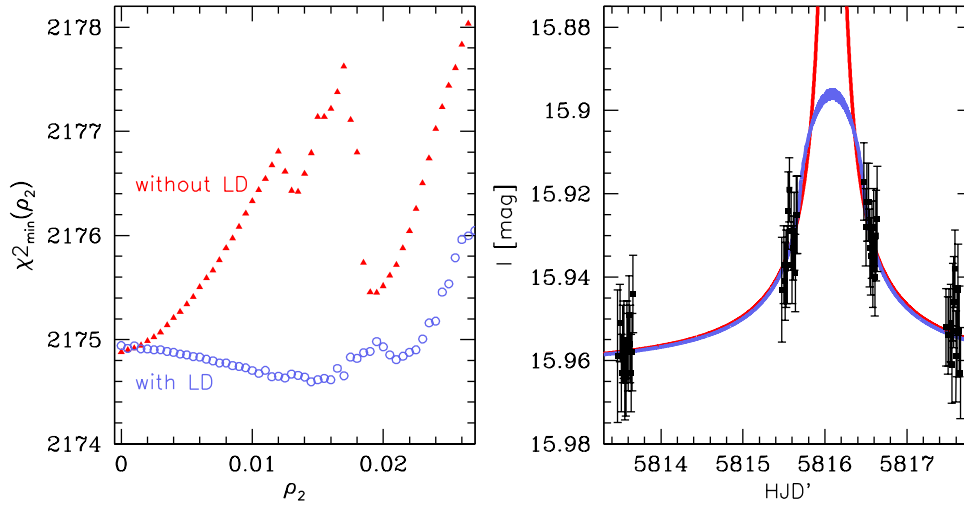


Figure 2. Degeneracy in ρ_2 for binary source model. *Left panel* shows minimum χ^2 calculated in bins of ρ_2 that are 0.0005 wide. Solid red triangles present models without limb darkening, and one can see that at $\rho_{2,\text{lim}} = 0.0174$ the χ^2 shows a local maximum. This produces a discrete degeneracy in ρ_2 . After including limb darkening (open blue circles) the degeneracy effectively disappears. Both curves monotonically rise for ρ_2 values larger than plot limits. *Right panel* shows the corresponding light curves zoomed in on the anomaly. The blue curve is the same as in Figure 1.

Table 1. Binary source model parameters

Parameter	value
(1)	(2)
$t_{0,1}$	5689.189 ± 0.044
$u_{0,1}$	0.852 ± 0.039
t_E (d)	29.18 ± 0.86
$t_{0,2}$	5816.100 ± 0.072
$u_{0,2}$	$0.0079^{+0.0063}_{-0.0047}$
ρ_2	$0.0209^{+0.0097}_{-0.0123}$
$F_{s,1}/F_{\text{base}}^a$	$0.821^{+0.079}_{-0.065}$
$F_{s,2}/F_{\text{base}}^a$	$5.36^{+0.75}_{-0.60} \times 10^{-4}$
$\chi^2/d.o.f.$	2174.60/2922

^a $F_{s,1}$ and $F_{s,2}$ denote fluxes of the two sources, and F_{base} denotes the baseline flux (all in the I band).

source or to the lens, a star that is not connected to either of them, or any combination of those possibilities.

In order to verify the double-source model we checked for the chromatic effect predicted by [Gaudi \(1998\)](#), and we discuss this possibility below.

The posterior proper motion distribution without Galactic priors is very wide: $\mu = 0.53^{+13.1}_{-0.39}$ mas yr⁻¹, hence, even if we wait many years and use high angular resolution observations, we may not be able to

resolve the lens and source and thus infer the proper motion. Resolving the two source components is currently beyond the capabilities of existing telescopes. Therefore, we conclude that continuous, higher-cadence, and higher-precision observations of such anomalies are crucial for proving the double-source model. Namely, more data would have provided a higher χ^2 difference between the different models, helped to verify whether both subevents have the same source color, and better constrained the relative proper motion for future verification via high-resolution imaging (Gaudi 1998).

3.2. Binary lens model

The main parameters describing the binary lens models are q (the mass ratio of the lens components) and s (the projected separation relative to θ_E). Binary lenses produce a set of closed curves called caustics, on which a point source would have infinite magnification. Depending on s and q , the number of caustics can be one, two, or three (Schneider & Weiss 1986). We can exclude topologies with a single caustic, as they cannot produce PSPL light curves with a subevent as observed here. The small ratio of timescales for both subevents in OGLE-2011-BLG-0173 strongly suggests a small mass ratio: $q \approx (t_{E,2}/t_{E,1})^2 \approx (1 \text{ d}/30 \text{ d})^2 \approx 0.0011$. The long time difference between subevents (Δt) suggests a large value of projected separation: $s \approx \Delta t/t_E = 4.3$. For the binary lens model, we assumed a limb-darkening coefficient of $u = 0.64$ based on the preliminary fitted model and Claret & Bloemen (2011).

Despite the above arguments, we ran an intensive MULTINEST simulation to ensure that all the degenerate solutions were found. To our surprise, two families of degenerate models were identified – see Figure 3. First, the planetary model that we expected: $s \approx 4.6$ (wide solution) and $q \approx 0.0005$ that produces two caustics, with the source approaching the planetary caustic, which causes the anomaly. The source can pass both caustics on the opposite or same sides (Gaudi & Gould 1997); we denote these models wide-A and wide-B, respectively. The corresponding models differ significantly in only one parameter: the angle between source trajectory and binary lens axis (α). Both models show continuous degeneracy in ρ . For wide-A the best χ^2 solution has $\rho \approx 0.09$, while for wide-B $\rho \approx 0.016$. Second, we found a solution with $s \approx 0.22$ (close solution) and $q \approx 0.014$ that produces

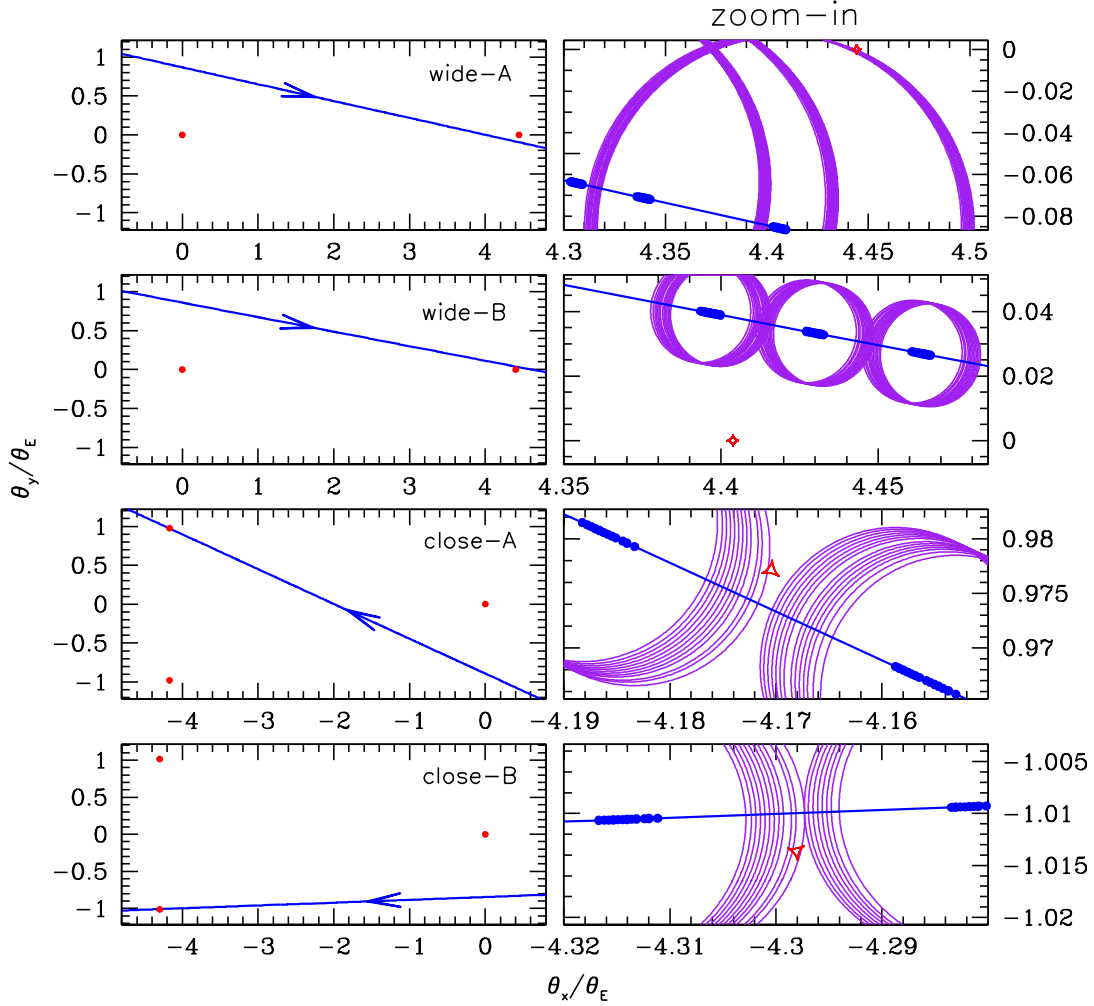


Figure 3. Source trajectories and caustics of OGLE-2011-BLG-0173 for different binary lens models (one per row). Each row shows all caustics (large red dots) in the left column and zoom-in on the trajectory close to the caustic responsible for the short-timescale anomaly in the right column. The arrows mark the direction of the source motion. In the right column, the large blue dots mark the positions of the source during two or three nights close to the peak of anomaly, and the purple rings mark the source perimeter for each epoch.

a central caustic and two planetary caustics, where a close approach to one of the two planetary caustics creates the anomaly. This family also further divides into two separate modes with the source crossing the binary axis between planetary and central caustics (close-A), or beyond the central caustic (close-B). The distance between planetary and central caustics projected on a binary axis is $|s - s^{-1}|$ (Han 2006) and the better approximation is $s(1 + q)^2 - (s(1 + q)^2)^{-1}$ (Bozza 2000). Hence, $s \approx 4.6$ and $s \approx 0.22$ give similar values of the caustics distance. The degeneracy between these two families of models was not known before: Gaudi & Gould (1997) explored anomalies in the light curves of planetary microlensing events and found that the shapes of anomalies are different for $s > 1$ and $s < 1$ at fixed q . This degeneracy is similar in spirit, although more general, to the degeneracy between a close binary lens with orbital motion and a circumbinary planet (Bennett et al. 1999; Albrow et al. 2000; Jung et al. 2013). The new degeneracy is present in OGLE-2011-BLG-0173 because of poor sampling of the anomaly. The anomalies in the close solution have smaller amplitude for given q , hence, significantly larger q is needed for the close model to produce the anomaly light curve similar to that of the wide model. In a typical situation for small values of q and $s < 1$ the anomaly is observed when the source passes between the caustics through a demagnification region (e.g., Sumi et al. 2010), which is absent in the $s > 1$ case.

The parameters of the fitted models are presented in Table 2. The last two rows of the table present χ^2 per degree of freedom and the Bayesian evidence relative to the close-A model as returned by MultiNest.

Models presented above predict different brightnesses at the peak of the anomaly. Distributions of I -band peak brightness are plotted in Figure 4. The range of peak brightness is wide for binary source and close binary lens models. The wide binary lens models predict a narrow range of peak brightness. Figure 4 shows that a single brightness measurement at the peak of the anomaly would not be enough to fully resolve the degeneracy. Once more we see that continuous coverage of planetary anomaly would help resolve the degenerate models.

3.3. *Source properties*

Table 2. Binary lens models parameters

Parameter	wide-A	wide-B	close-A	close-B
(1)	(2)	(3)	(4)	(5)
t_0	5689.190 ± 0.043	5689.190 ± 0.043	5689.211 ± 0.045	5689.139 ± 0.045
u_0	0.850 ± 0.036	0.851 ± 0.037	0.817 ± 0.035	0.844 ± 0.038
t_E (d)	29.20 ± 0.80	29.19 ± 0.82	30.15 ± 0.83	29.37 ± 0.86
ρ	0.064 ± 0.039	0.070 ± 0.042	$0.0199^{+0.0089}_{-0.0116}$	$0.0205^{+0.0084}_{-0.0108}$
α (deg)	$168.05^{+0.35}_{-0.41}$	$169.86^{+0.41}_{-0.40}$	$335.10^{+1.28}_{-1.55}$	$3.21^{+1.66}_{-1.35}$
s	4.66 ± 0.12	4.63 ± 0.13	0.2220 ± 0.0056	$0.2167^{+0.0057}_{-0.0061}$
q	0.00046 ± 0.00014	0.00042 ± 0.00015	$0.0144^{+0.0034}_{-0.0025}$	$0.0151^{+0.0040}_{-0.0028}$
F_s/F_{base}^a	$0.818^{+0.073}_{-0.061}$	$0.818^{+0.073}_{-0.064}$	$0.755^{+0.065}_{-0.055}$	$0.805^{+0.078}_{-0.062}$
$\chi^2/d.o.f.$	2172.30/2922	2173.54/2922	2167.03/2922	2173.15/2922
$Z/Z_{\text{close-A}}^b$	0.0321	0.0169	1.0000	0.0422

NOTE—The parameter conventions follow Skowron et al. (2011) except t_0 and u_0 which are measured relative to the higher-mass lens component.

^aSource flux to baseline flux in I band.

^bBayesian evidence relative to the close-A solution.

The physical scale of the microlensing event is set by the Einstein ring radius $\theta_E = \theta_\star/\rho$. The value of the angular source radius θ_\star is estimated here twice. First, for the source in the binary lens model ($\theta_{\star,1}$) and second, for the second source ($\theta_{\star,2}$) in the binary source model.

To derive θ_\star for the binary lens model, we follow the method presented by Yoo et al. (2004). Figure 5 presents the CMD for the stars close to the event. The measured properties of the red clump (RC) centroid are: $(V - I)_{\text{RC}} = 2.556 \pm 0.006$ mag and $I_{\text{RC}} = 16.048 \pm 0.016$ mag. The

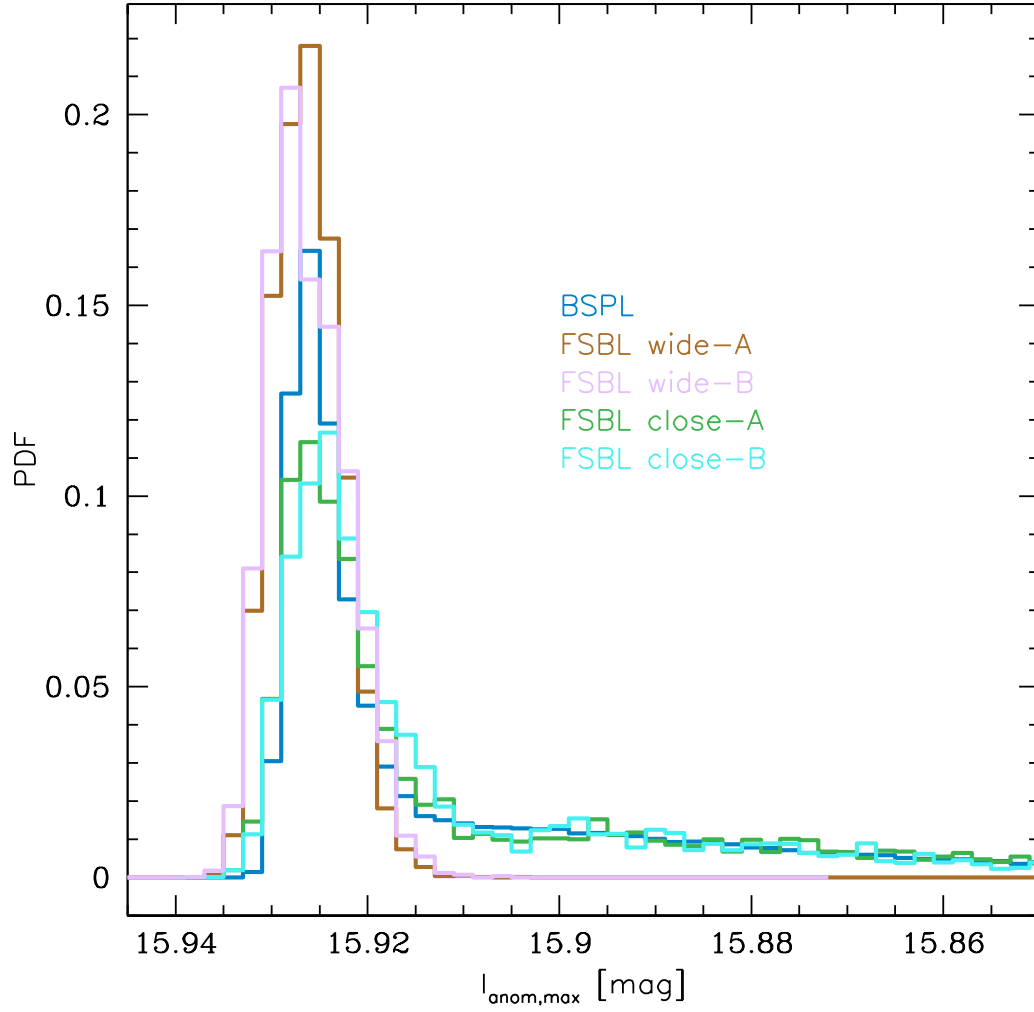


Figure 4. Probability distribution of peak brightness during the anomaly for five different models.

extinction-free parameters of the RC centroid are: $(V - I)_{\text{RC},0} = 1.06$ mag (Bensby et al. 2011) and $I_{\text{RC},0} = 14.375$ mag (Table 2 of Nataf et al. 2013). By comparing the above values, we find the

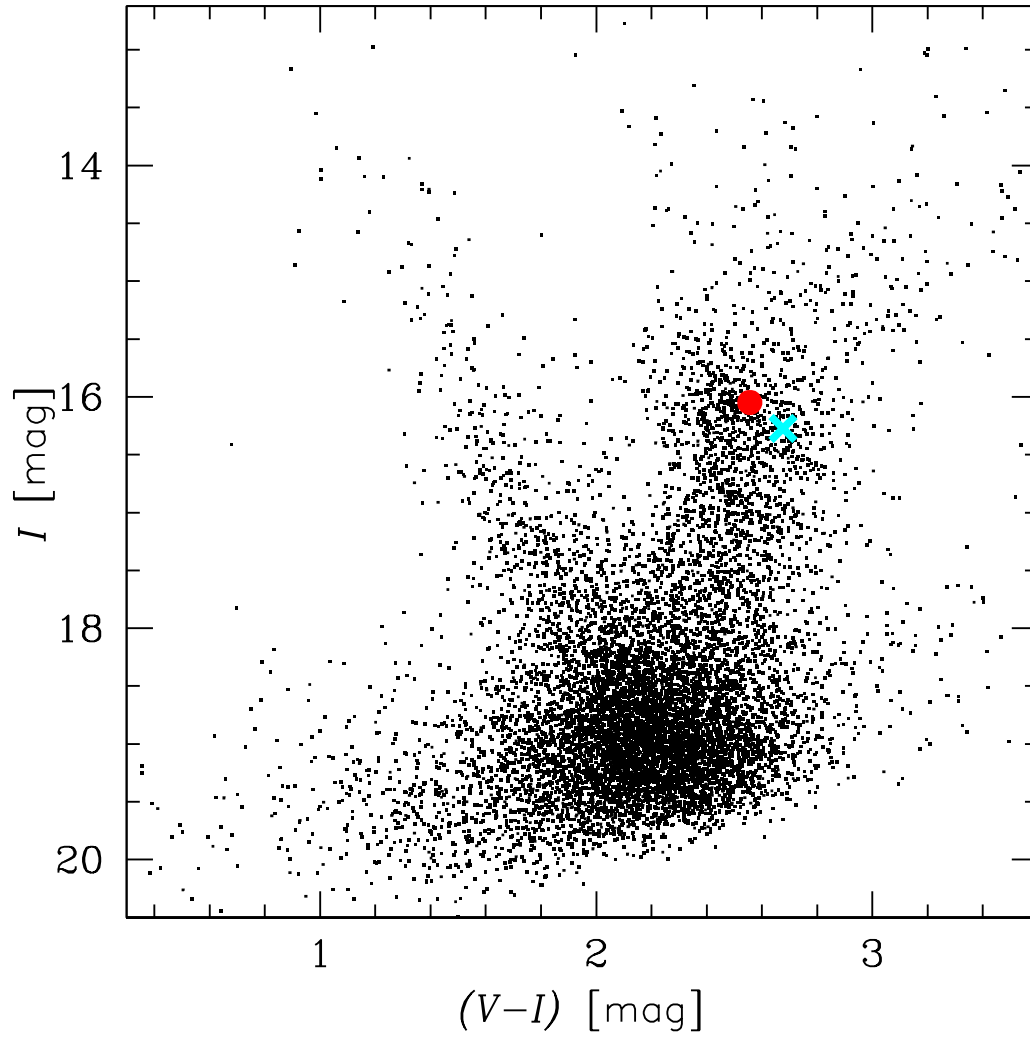


Figure 5. Color-magnitude diagram for stars within $2'$ from the event. Red circle marks the red clump centroid. The cyan cross marks the source position.

reddening and the extinction of $E(V-I) = 1.496$ mag and $A_I = 1.673$ mag. The source unmagnified

brightness ($I_s = 16.272$ mag and $V_s = 18.949$ mag) is corrected for extinction: $I_{s,0} = 14.599$ mag and $V_{s,0} = 15.780$ mag. The extinction-free magnitudes correspond to the near-infrared brightness of $K_{s,0} = 13.063$ mag which we calculated using the intrinsic colors of giant stars (Bessell & Brett 1988). After applying the Kervella et al. (2004) relation between $(V - K)$ color and the surface brightness, we obtain $\theta_{*,1} = 7.50_{-0.11}^{+0.23}$ μas . For consistency of the results, the above procedure, which effectively translates (I_s, V_s) to $\theta_{*,1}$, was repeated for every model in the posterior distributions. Based on that, we derive the following values of θ_E : $0.36_{-0.25}^{+3.03}$ mas for wide-A, $0.33_{-0.24}^{+2.43}$ mas for wide-B, $0.79_{-0.46}^{+4.36}$ mas for close-A, and $0.76_{-0.43}^{+4.71}$ mas for close-B model.

For the binary source model we cannot use the Yoo et al. (2004) method, because only single-band photometry is available for the anomaly. Instead, we derive the angular source radius by combining the measured source flux and the stellar isochrones. The source distance modulus is $DM_s = 14.481$ mag based on the mean bulge distance as a function of Galactic longitude (Nataf et al. 2013). Thus, the first-source absolute brightness is $M_{I,s} = 0.118$ mag. The flux ratio of the source components corresponds to 8.18 mag, hence, the absolute brightness of the second source is $M_{I,s2} = 8.29$ mag. We extracted the radii for dwarfs (age of 10 Gyr, $[\text{Fe}/\text{H}] = -1$, and $Y = 0.27$) from Dotter et al. (2008) isochrones. The radius, combined with the source distance, leads to $\theta_{*,2} = 0.2282 \pm 0.0096$ μas and $\theta_E = 0.042_{-0.031}^{+1.041}$ mas.

4. INTERPRETATION

The analysis of the microlensing light curve leads us to five different scenarios that could produce the observed signal: single lens with binary source or four different scenarios of binary lens with a single source. Two binary lens scenarios have (s, q) of $(4.6, 0.0005)$ and the other two of $(0.22, 0.014)$. We compare these different scenarios by combining Bayesian evidence extracted from MULTINEST runs with priors from the Galactic model and statistical properties of microlensing planetary systems.

In order to constrain the prior probabilities, we used the modified version of the Galactic model by Clanton & Gaudi (2014, see there for details). The lenses are main-sequence stars drawn from density profiles of a double-exponential disk and a boxy Gaussian bulge. The parameters of the main-sequence mass function are taken from model 1 of Sumi et al. (2011). The source distance

Table 3. Posterior physical parameters statistics

Parameter	BSPL	FSBL wide-A	FSBL wide-B	FSBL close-A	FSBL close-B
(1)	(2)	(3)	(4)	(5)	(6)
$\Gamma/\Gamma_{\text{close-A}}$...	0.397	0.382	1.000	1.093
μ (mas yr ⁻¹)	4.2 ^{+2.7} _{-1.8}	4.3 ^{+2.6} _{-1.8}	4.7 ^{+2.6} _{-1.9}	4.6 ^{+2.7} _{-1.2}	4.7 ^{+2.5} _{-1.2}
D_l (kpc)	6.2 ^{+1.3} _{-1.7}	6.1 ^{+1.3} _{-1.7}	6.0 ^{+1.3} _{-1.7}	5.9 ^{+1.2} _{-1.6}	5.9 ^{+1.2} _{-1.6}
M_l (M _⊙)	0.40 ^{+0.30} _{-0.21}	0.41 ^{+0.30} _{-0.21}	0.42 ^{+0.29} _{-0.22}	0.43 ^{+0.28} _{-0.21}	0.43 ^{+0.28} _{-0.21}
M_c (M _{Jup})	...	0.19 ^{+0.18} _{-0.11}	0.18 ^{+0.17} _{-0.10}	6.5 ^{+4.8} _{-3.2}	6.8 ^{+5.1} _{-3.4}
r_E (AU)	1.91 ^{+0.80} _{-0.65}	1.96 ^{+0.80} _{-0.65}	2.04 ^{+0.78} _{-0.68}	2.12 ^{+0.68} _{-0.50}	2.12 ^{+0.67} _{-0.50}
\hat{r}_E (AU)	2.7 ^{+1.6} _{-1.2}	2.9 ^{+1.6} _{-1.2}	3.0 ^{+1.6} _{-1.2}	3.09 ^{+1.57} _{-0.79}	3.06 ^{+1.45} _{-0.77}

NOTE—The parameters are: $\Gamma/\Gamma_{\text{close-A}}$ – event rate relative to FSBL close-A model, μ – relative lens-source proper motion, D_l – lens distance, M_l – lens mass, M_c – mass of lens companion (if present), r_E – Einstein ring radius (in lens plane), and \hat{r}_E – Einstein ring radius projected on the source plane.

is drawn from the boxy Gaussian bulge distribution (model G2 in [Dwek et al. 1995](#)). The relative proper motion cutoff was increased to 80 mas yr⁻¹ in each coordinate. To set the priors, we use only the marginalized event rate $d^2\Gamma/dt_E d\theta_E$.

We combined the estimates of $\theta_{\star,1}$ and $\theta_{\star,2}$, the measured parameters, and Γ values to derive posterior statistics of physical event parameters. These statistics are presented in Table 3 for binary source and all binary lens models. The Einstein ring radius in linear units (r_E) values for binary lens models lead to projected separations on the order of 8 AU and 0.5 AU for wide and close models, respectively. The ice line is at a distance of $\sim 2.7(M_l/M_\odot)$ AU = 1.1 AU ([Kennedy & Kenyon 2008](#)), i.e., a few times closer to the star than the planet in the wide solution.

The parameters t_E and θ_E were estimated for each model in the posterior distributions, thus allowing integration of Γ over posterior distributions via importance sampling. In Table 3 we provide event rates relative to the close-A model.

The prior on binary lens models additionally depends on the planet properties. The statistical properties of microlensing planets were derived by Suzuki et al. (2016) using MOA survey data and combined with earlier results by Gould et al. (2010) and Cassan et al. (2012). The planet mass ratio and separation function is:

$$\frac{d^2 N_{\text{pl}}}{d \log q d \log s} = A \left(\frac{q}{1.7 \times 10^{-4}} \right)^n s^m \quad (1)$$

where $A = 0.61^{+0.21}_{-0.16}$, $m = 0.49^{+0.47}_{-0.49}$, and $n = -0.93 \pm 0.13$ for $q > 1.7 \times 10^{-4}$ and $n = 0.6^{+0.5}_{-0.4}$ otherwise. The sensitivity of the Suzuki et al. (2016) study to planets similar to our wide model is low, but this study gives the best information we can currently use as a prior. The uncertainty of the coefficient A is large, but it is not important when different binary lens models are compared. Integrating the above function results in:

- $N_{\text{pl,wide-A}}/N_{\text{pl,close-A}} = 178$
- $N_{\text{pl,wide-B}}/N_{\text{pl,close-A}} = 212$
- $N_{\text{pl,close-B}}/N_{\text{pl,close-A}} = 0.952$

We multiply the microlensing event rate (Table 3), the planet mass ratio and separation functions (above), and the Bayesian evidence (Table 2) to find the posterior odds:

- wide-A to close-A: 2.27,
- wide-B to close-A: 1.37,
- close-B to close-A: 0.044.

Hence, the wide-A model is preferred. The posterior odds for the wide model family relative to the close model family are 3.5. The preference for wide models over the close models comes mostly from the Suzuki et al. (2016) prior. Simply put: we know from previous microlensing surveys that, for

planets beyond the snow-line (i.e., $s \gtrsim 0.3$), low-mass planets are much more abundant than high-mass planets, and we assume that this holds also for wide-orbit planets. Most of the preference in the [Suzuki et al. \(2016\)](#) prior for wide models comes from the mass ratio, not the separation itself. The notion that the planets with the smallest mass ratios are more common than the higher mass ratio ones was confirmed by a joint analysis of microlensing, as well as radial velocity and direct imaging data – see [Clanton & Gaudi \(2016\)](#).

It is much more difficult to compare the binary source model versus the binary lens model priors. Both models have three of the same parameters that constrain the main subevent (t_0 , u_0 , and t_E) but differ in other ones: four for the binary lens (ρ , α , s , and q) vs. three for the binary source ($t_{0,2}$, $u_{0,2}$, and ρ_2). We compare binary lens and binary source models below.

Binary lens models fit the observed light curve better than the binary source model with a χ^2 difference of 2.30 and 7.57 relative to the close and wide family of models, respectively. According to [Suzuki et al. \(2016\)](#), $d^2 N_{\text{pl}} / (\log q \, d \log s) \approx 0.5$ for the wide model. Also, stellar companions are present around half of the stars ([Raghavan et al. 2010](#)) but this includes all separations and mass ratios. Below we discuss the probability of a companion with the projected separation and mass ratio inferred for binary source models.

The projected separation of binary source components is $\sqrt{\left(\frac{t_{0,2}-t_{0,1}}{t_E}\right)^2 + u_{0,1}^2} = 4.4$ times \hat{r}_E (Einstein ring radius projected on the source plane). The \hat{r}_E is $2.7_{-1.2}^{+1.6}$ AU for the double-source model, leading to a very wide distribution of binary source projected separations. The first source is close to the RC on the CMD, and we may guess that the first-source mass is similar to that of typical RC stars, which is on the order of $0.9 M_\odot$. The mass of the RC stars was estimated based on [Nataf et al. \(2012\)](#) and the mass-loss rates from [Miglio et al. \(2012\)](#). The isochrones suggest the secondary source mass of $0.35 M_\odot$, hence, the total mass of the binary source is $1.25 M_\odot$ and the mass ratio is 0.4. The mean value of \hat{r}_E multiplied by 4.4, corrected for a projection factor of $\sqrt{3/2}$, and combined with the total mass of the system results in an orbital period of 52 years or $\log P$ [day] = 4.3. This is close to the peak of period distribution of local binary systems derived by [Raghavan et al.](#)

(2010) of 5.0 ± 2.3 . Thus, the inferred properties of the binary source are not, considered in isolation, particularly unusual.

Nevertheless, our analysis suggests that a binary lens model is more probable than the binary source model, because the source can pass farther away from the planetary caustic to produce the observed signal than the lens can pass from the second source. In other words, we find that the prior phase space to produce the secondary signal seen is considerably larger for the single source binary lens model than for the binary source single lens model. To quantify this argument, we selected all the wide binary lens and binary source models with $\Delta\chi^2 < 9$ relative to the best-fitting model in each group. For each model we calculated the minimum approach distance to the planetary caustic or the second source and divided it by the distance from the primary lens/source. The range of derived values is larger by a factor of 3.9 for the binary lens model than for the binary source model, indicating that the source can pass considerably farther away from the planetary caustic than the lens can pass from the secondary source to produce the observed signal.

We combine the binary source orbital period and assume a circular orbit to derive the brighter component radial velocity semi-amplitude of $K \sim 2.3 \sin i \text{ km s}^{-1}$, which can be detected by the long-term spectroscopic follow-up. However, the range of orbital periods, and hence radial velocity semi-amplitude, is wide and inclination is unknown. The lack of detection of change in the radial velocity would not necessarily be conclusive in deciding whether the binary lens or the binary source model is true.

Assuming heretofore that the wide binary lens model is the correct one, there is only one microlensing planet with a larger inferred value of s : OGLE-2008-BLG-092LAb. The binary lens versus binary source degeneracy was resolved for OGLE-2008-BLG-092 using the light-curve analysis alone but was based on two important factors: the presence of a third microlensing body in that system, and the fact that the planetary subevent amplitude was larger than the host subevent amplitude (Poleski et al. 2014).

Two other events suffer from a severe degeneracy caused by poor coverage of the anomaly observed far from the peak of the event: MACHO-97-BLG-41 (Bennett et al. 1999; Albrow et al. 2000; Jung

et al. 2013) and OGLE-2013-BLG-0723 (Udalski et al. 2015b; Han et al. 2016). In both these cases the degeneracy was between the binary lens with an orbital motion and the static triple lens models.

The lack of multiband photometry during the anomaly prevents us from conclusively distinguishing between the binary lens and binary source model based on the chromaticity of the light curve (Gaudi 1998). For binary lens models we can predict brightness at the peak of the anomaly directly and obtain $(V - I)$ of 2.342 ± 0.002 mag for the wide model and 2.353 ± 0.023 mag for the close model. For the binary source we derived the second-source brightness from the above analysis of the source properties and found observed $(V - I)$ color of 3.457 for fiducial properties of the second source. This allows us to predict $(V - I)$ color at the peak of the anomaly of 2.195 ± 0.043 mag. The color estimates do not use Galactic model priors but take full account of the blending flux. We expect the $(V - I)$ color difference of 0.147 mag, which could have been measured if V -band photometry had been obtained during the anomaly.

5. ICE GIANT OCCURRENCE RATES

Here we present an attempt to investigate statistical properties of microlensing planets on wide orbits using currently available data. In Figure 6 we show mass ratio versus projected separation (i.e., the quantities that are measured directly) for all low-mass companions with $s > 2$. We see that at the very wide orbits, the companions seem to separate into groups: two objects have $q > 0.016$, two others have $q < 1.5 \times 10^{-4}$ and there are no objects detected with mass ratios in between. In order to quantitatively assess the number of objects with different properties, we divided the detected low-mass companions with separations in the $3.5 < s < 5.5$ range into three bins: $10^{-4} < q < 10^{-3}$, $10^{-3} < q < 10^{-2}$, and $10^{-2} < q < 4 \times 10^{-2}$. These bins are marked in Figure 6 by thick red, long-dashed blue, and short-dashed pink rectangles, respectively. We integrated the sensitivity of two recent statistical analyses of survey data: Tsapras et al. (2016) for OGLE-III and Suzuki et al. (2016) for MOA-II, which searched 2433 and 1474 events, respectively. Integration was done in each bin separately, assuming one companion for each star with given properties. Tsapras et al. (2016) showed their results in physical projected separation and companion mass, which we translated back to (s, q) assuming $r_E = 2.3$ AU and $M_l = 0.4 M_\odot$. In Table 4 we present how many objects each of

these surveys would detect under our assumptions and how many were in fact detected. Additionally, we give the number of objects currently known in each bin from all microlensing detections. The sensitivity of all microlensing detections is not known, but it is obviously decreasing with decreasing mass ratio.

There are just a few detections of objects in the considered separation range, which prevent us from drawing definitive conclusions. We note that there are many events that were searched for distant companions, which resulted in only four detections altogether: on order of 20,000 events alerted by the OGLE and MOA surveys, in addition to the [Tsapras et al. \(2016\)](#) and [Suzuki et al. \(2016\)](#) samples. The numbers presented in Table 4 suggest that companions in the lowest mass ratio range are common (see also [Foreman-Mackey et al. 2016](#)). We can consider them as analogs of Uranus and Neptune. In the highest mass ratio bin, the frequency of objects seems significantly smaller. These objects likely did not form in a protoplanetary disk around the primary star and hence probably should be considered brown dwarfs – see the discussion in [Poleski et al. \(2017\)](#) and [Bryan et al. \(2017\)](#) for more details. Note that OGLE-2014-BLG-1112 with $q = 0.028$ and $s = 2.4$ has a direct mass measurement of $0.03 M_{\odot}$, i.e., in the brown dwarf range.

The intermediate mass ratio range $10^{-3} < q < 10^{-2}$ has no detections, and it is possible that the occurrence rate of these objects is similar to the occurrence $10^{-2} < q < 4 \times 10^{-2}$ range. If future data show that the occurrence rate in the intermediate mass ratio bin is indeed lower, then in the lowest mass ratio bin, than this would indicate the existence of a massive ice giant desert. The objects with $10^{-3} < q < 10^{-2}$ have masses of a few M_{Jup} , but are on much wider orbits. For in-situ formation, the lack of such planets is naturally understood in the core-accretion planet formation model (e.g., [Pollack et al. 1996](#)). Protoplanetary disks are likely simply not massive enough and the dynamical times are too long at such wide orbits to form Jupiter- or higher-mass planets.

6. SUMMARY

We have presented the analysis of microlensing event OGLE-2011-BLG-0173. The event is clearly anomalous, but the physical cause of the anomaly is not uniquely determined. There are two distinct sets of models. The first is a single source and a binary lens, which itself has two families of solutions:

Table 4. Occurrence rates

sample	$10^{-4} < q < 10^{-3}$		$10^{-3} < q < 10^{-2}$		$10^{-2} < q < 4 \times 10^{-2}$	
	detected	expected	detected	expected	detected	expected
(1)	(2)	(3)	(4)	(5)	(6)	(7)
Tsapras et al. (2016)	1	4.1	0	28.	0	91.
Suzuki et al. (2016)	0	1.0	0	7.9	1	52.
all detections	2 ^a	...	0	...	2	...

^aHere we assume the wide model is correct for OGLE-2011-BLG-0173.

a less massive companion with a larger projected separation, or a more massive companion with a smaller projected separation. We demonstrated, using the [Suzuki et al. \(2016\)](#) mass ratio and separation function as a prior, that the wide-orbit planet model is more probable. Unfortunately, we cannot fully distinguish between the binary lens and binary source models, though our considerations support the binary lens model. Each of these scenarios demonstrated degeneracies that were uncovered for the first time. We found that the best way for resolving all of these degeneracies in future events is to collect continuous, high-cadence photometry, preferably with relatively frequent observations in a second band (at least once per day when $q > 10^{-4}$ planets are considered). This is essentially the strategy that will be employed by the WFIRST microlensing survey. The KMTNet survey employs a similar strategy (e.g., [Kim et al. 2018a](#)), but its observations are affected by weather.

The detailed Bayesian analysis provided a resolution of the model-fitting degeneracies. In our opinion, more advanced methods, such as the hierarchical Bayesian analysis, should be more commonly used in analyzing microlensing events.

We have also analyzed the set of known low-mass microlensing companions with large projected separations. If OGLE-2011-BLG-0173 is in fact a binary lens event with a wide-orbit planet, then it

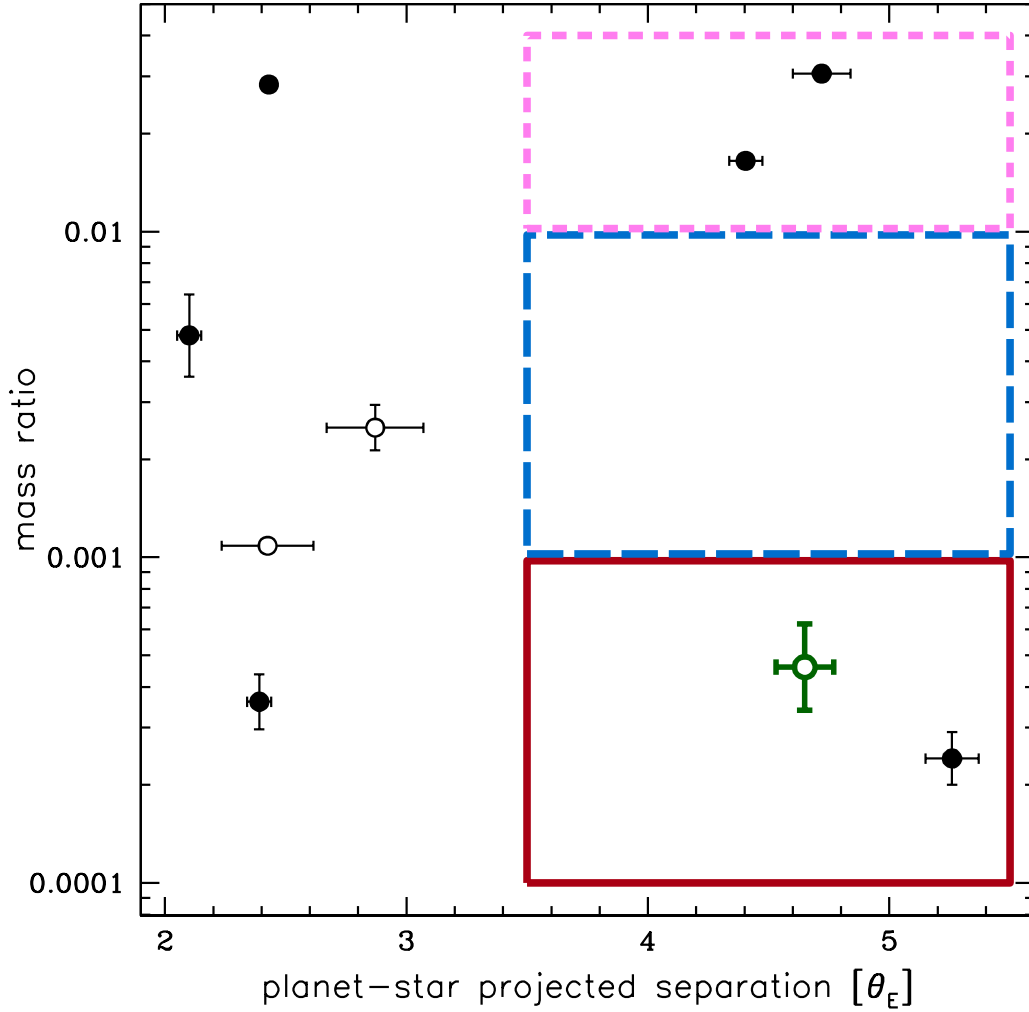


Figure 6. Mass ratio vs. projected separation plot for microlensing detections with $s > 2$. Open symbols represent objects that suffer wide–close (or s vs. s^{-1}) degeneracy, while full symbols represent objects that are not affected by the wide–close degeneracy. Green thick point represents OGLE-2011-BLG-0173. The three rectangles show limits used for integrating detection efficiencies – see Table 4. The events shown are from the highest to the lowest mass ratio: OGLE-2016-BLG-0263 (Han et al. 2017a), OGLE-2014-BLG-1112 (Han et al. 2017b), MOA-2012-BLG-006 (Poleski et al. 2017), MOA-bin-1 (Bennett et al. 2012), MOA-2007-BLG-400 (Dong et al. 2009), OGLE-2012-BLG-0563 (Fukui et al. 2015), OGLE-2011-BLG-0173 (this paper), MOA-2013-BLG-605 (Sumi et al. 2016), and OGLE-2008-BLG-092 (Poleski et al. 2014).

is only the second low-mass planet on a very wide orbit detected. Current surveys have low detection efficiency for wide-orbit planets and resulted in two planet detections, suggesting that the wide-orbit planets are not rare. There are two other events with wide-orbit companions but their mass ratios are larger by 1.5 dex, suggesting that they, perhaps, are more likely binary, rather than planetary companions. The observed lack of detections in intermediate mass ratios may be interpreted as tentative evidence for a massive ice giant desert.

Authors would like to thank Prof. A. Gould for consultation, C. Clanton for support in preparing Galactic models, and S. Johnson for comments on manuscript. We thank the anonymous referee, whose comments helped to clarify the text. OGLE Team acknowledges Profs. M. Kubiak and G. Pietrzyński, former members of the team, for their contribution to the collection of the OGLE photometric data over the past years. This work was partially supported by NASA contract NNG16PJ32C. The OGLE project has received funding from the National Science Centre, Poland, grant MAESTRO 2014/14/A/ST9/00121 to A.U. This research made use of *ASTROPY*, a community-developed core Python package for Astronomy ([Astropy Collaboration et al. 2013](#)).

Software: MultiNest ([Feroz & Hobson 2008](#); [Feroz et al. 2009](#)), SM Numerical Recipes ([Press et al. 1992](#))

REFERENCES

- Alard, C. 2000, *A&AS*, 144, 363
- Albrow, M. D., Beaulieu, J.-P., Caldwell, J. A. R., et al. 2000, *ApJ*, 534, 894
- Astropy Collaboration, Robitaille, T. P., Tollerud, E. J., et al. 2013, *A&A*, 558, A33
- Bennett, D. P., Rhie, S. H., Becker, A. C., et al. 1999, *Nature*, 402, 57
- Bennett, D. P., Sumi, T., Bond, I. A., et al. 2012, *ApJ*, 757, 119
- Bensby, T., Adén, D., Meléndez, J., et al. 2011, *A&A*, 533, A134
- Bessell, M. S., & Brett, J. M. 1988, *PASP*, 100, 1134
- Bond, I. A., Abe, F., Dodd, R. J., et al. 2001, *MNRAS*, 327, 868
- Bozza, V. 2000, *A&A*, 355, 423

- Bryan, M. L., Benneke, B., Knutson, H. A., Batygin, K., & Bowler, B. 2017, *Nature Astronomy*, doi:10.1038/s41550-017-0325-8
- Cassan, A., Kubas, D., Beaulieu, J.-P., et al. 2012, *Nature*, 481, 167
- Clanton, C., & Gaudi, B. S. 2014, *ApJ*, 791, 90
- . 2016, *ApJ*, 819, 125
- Claret, A., & Bloemen, S. 2011, *A&A*, 529, A75
- Dong, S., Bond, I. A., Gould, A., et al. 2009, *ApJ*, 698, 1826
- Dotter, A., Chaboyer, B., Jevremović, D., et al. 2008, *ApJS*, 178, 89
- Dwek, E., Arendt, R. G., Hauser, M. G., et al. 1995, *ApJ*, 445, 716
- Feroz, F., & Hobson, M. P. 2008, *MNRAS*, 384, 449
- Feroz, F., Hobson, M. P., & Bridges, M. 2009, *MNRAS*, 398, 1601
- Foreman-Mackey, D., Morton, T. D., Hogg, D. W., Agol, E., & Schölkopf, B. 2016, *AJ*, 152, 206
- Fukui, A., Gould, A., Sumi, T., et al. 2015, *ApJ*, 809, 74
- Gaudi, B. S. 1998, *ApJ*, 506, 533
- Gaudi, B. S., & Gould, A. 1997, *ApJ*, 486, 85
- Goldreich, P., Lithwick, Y., & Sari, R. 2004, *ARA&A*, 42, 549
- Gould, A. 1994, *ApJL*, 421, L71
- . 2000, *ApJ*, 542, 785
- Gould, A., Dong, S., Gaudi, B. S., et al. 2010, *ApJ*, 720, 1073
- Griest, K., & Hu, W. 1992, *ApJ*, 397, 362
- Han, C. 2006, *ApJ*, 638, 1080
- Han, C., Bennett, D. P., Udalski, A., & Jung, Y. K. 2016, *ApJ*, 825, 8
- Han, C., Udalski, A., Gould, A., et al. 2017a, *AJ*, 154, 133
- Han, C., Udalski, A., Bozza, V., et al. 2017b, *ApJ*, 843, 87
- Jung, Y. K., Han, C., Gould, A., & Maoz, D. 2013, *ApJL*, 768, L7
- Kane, S. R. 2011, *Icarus*, 214, 327
- Kennedy, G. M., & Kenyon, S. J. 2008, *ApJ*, 673, 502
- Kervella, P., Bersier, D., Mourard, D., et al. 2004, *A&A*, 428, 587
- Kim, D.-J., Kim, H.-W., Hwang, K.-H., et al. 2018a, *AJ*, 155, 76
- Kim, H.-W., Hwang, K.-H., Kim, D.-J., et al. 2018b, *AJ*, 155, 186
- Kim, S.-L., Lee, C.-U., Park, B.-G., et al. 2016, *Journal of Korean Astronomical Society*, 49, 37
- Miglio, A., Brogaard, K., Stello, D., et al. 2012, *MNRAS*, 419, 2077
- Nataf, D. M., Gould, A., & Pinsonneault, M. H. 2012, *AcA*, 62, 33
- Nataf, D. M., Gould, A., Fouqué, P., et al. 2013, *ApJ*, 769, 88
- Paczynski, B. 1986, *ApJ*, 304, 1
- Penny, M. T., Gaudi, B. S., Kerins, E., et al. 2018, *ArXiv e-prints*, arXiv:1808.02490
- Poleski, R., Skowron, J., Udalski, A., et al. 2014, *ApJ*, 795, 42
- Poleski, R., Udalski, A., Bond, I. A., et al. 2017, *A&A*, 604, A103

- Pollack, J. B., Hubickyj, O., Bodenheimer, P., et al. 1996, *Icarus*, 124, 62
- Press, W. H., Teukolsky, S. A., Vetterling, W. T., & Flannery, B. P. 1992, *Numerical recipes in FORTRAN. The art of scientific computing*
- Raghavan, D., McAlister, H. A., Henry, T. J., et al. 2010, *ApJS*, 190, 1
- Schneider, P., & Weiss, A. 1986, *A&A*, 164, 237
- Skowron, J., Udalski, A., Gould, A., et al. 2011, *ApJ*, 738, 87
- Skowron, J., Udalski, A., Kozłowski, S., et al. 2016, *AcA*, 66, 1
- Spergel, D., Gehrels, N., Baltay, C., et al. 2015, e-print, arXiv:1503.03757
- Sumi, T., Bennett, D. P., Bond, I. A., et al. 2010, *ApJ*, 710, 1641
- Sumi, T., Kamiya, K., Bennett, D. P., et al. 2011, *Nature*, 473, 349
- Sumi, T., Udalski, A., Bennett, D. P., et al. 2016, *ApJ*, 825, 112
- Suzuki, D., Bennett, D. P., Sumi, T., et al. 2016, *ApJ*, 833, 145
- Thommes, E. W., Duncan, M. J., & Levison, H. F. 1999, *Nature*, 402, 635
- Tsapras, Y., Hundertmark, M., Wyrzykowski, L., et al. 2016, *MNRAS*, 457, 1320
- Tsiganis, K., Gomes, R., Morbidelli, A., & Levison, H. F. 2005, *Nature*, 435, 459
- Udalski, A. 2003, *AcA*, 53, 291
- Udalski, A., Szymański, M. K., & Szymański, G. 2015a, *AcA*, 65, 1
- Udalski, A., Jung, Y. K., Han, C., et al. 2015b, *ApJ*, 812, 47
- Woźniak, P. R. 2000, *AcA*, 50, 421
- Yoo, J., DePoy, D. L., Gal-Yam, A., et al. 2004, *ApJ*, 603, 139